Numerical prediction of impact damage in thick fabric composite laminates

van Hoorn, Niels; Turteltaub, Sergio; Kassapoglou, Christos; van den Brink, Wouter

DOI
10.1016/j.compstruct.2024.118726

Publication date
2025

Document Version
Final published version

Published in
Composite Structures

Composite Structures 353 (2025) 118726

Contents lists available at ScienceDirect

Composite Structures

journal homepage: www.elsevier.com/locate/compstruct

Numerical prediction of impact damage in thick fabric composite laminates

Niels van Hoorn [b,a,*], Sergio Turteltaub [b], Christos Kassapoglou [b], Wouter van den Brink [a]

[a] Royal Netherlands Aerospace Centre, Voorsterweg 31, 8316 PR Marknesse, The Netherlands
[b] Delft University of Technology, Faculty of Aerospace Engineering, Kluyverweg 1, 2629 HS Delft, The Netherlands

ARTICLE INFO

Keywords:
Thick composites
Impact behaviour
Finite Element Analysis (FEA)
Discrete Fracture Method
Cohesive Zone Model

ABSTRACT

A simulation methodology for assessing the damage in thick fabric Carbon Fibre Reinforced Polymer (CFRP) composite laminates under low- and high-velocity impacts is presented. It encompasses steps for calibration, verification, and validation of the elastic and fracture material properties as well as determination of model parameters for the numerical simulations. Damage is modelled using a discrete fracture approach with cohesive interface elements that capture individual cracks occurring in and between plies. For computational efficiency, the method is implemented in a two-dimensional (2D) axi-symmetric model. Results from double-cantilever beam, end-notched flexure, and quasi-static indentation experiments align well with numerical simulations and serve to calibrate and verify the implementation of the discrete fracture approach. The methodology is extended to dynamic impact analysis to predict damage mechanisms, force–displacement histories, and is validated using test results. This methodology combines meaningful insight in the failure mechanisms with a manageable computational effort, achieving a factor 50 improvement compared to a benchmark. A parametric analysis summarised in failure maps relates damage mechanisms to impact energy, mass, and laminate thickness. The proposed methodology strikes a balance between computational efficiency and accuracy, making it a valuable tool for optimum design and certification of thick CFRP composite laminates under impact.

1. Introduction

The substantial increase in use of composite materials in the aviation industry, particularly Carbon Fibre Reinforced Polymers (CFRP), is mainly attributed to their superior specific properties and the opportunities they offer for design compared to other materials used in the past. However, a limiting factor to further exploit the properties of CFRPs is directly related to design procedures that deal with damage. For instance, one requirement is that a composite structure should be able to carry loads under certain types of damage [1,2]. Especially impact-induced damage tolerance poses a significant challenge in composite design. Impacts can potentially occur at any point throughout the entire lifespan of a structure, by a wide variety of sources, including, for example, tool drops, hail, or runway debris. During such impact events, multiple damage mechanisms come into play, involving interactions among factors like delaminations, fibre breakage, and matrix cracking, which collectively yield a complex damage state. After an impact, a structure with damage up to Barely Visible Impact Damage (BVID) should still be able to endure ultimate loads without failing [1]. Due to the involvement of many design variables, material properties, and these complex damage mechanisms, extensive testing programs are necessary to assess the damage tolerance of composite structures. Therefore, there is a clear need for analysis methodologies and design tools that can complement existing testing and certification procedures. An approach that can predict the type, location, and extent of damage caused by impact can be used to predict the residual strength after impact [3,4].

The Finite Element Method (FEM) is widely employed for simulating impact damage, and substantial progress has been made in this area. Consequently, methodologies are now available that can provide accurate predictions regarding the response of relatively thin composite laminates subjected to low-velocity impacts, as supported by previous studies [5–11]. These methods typically utilise detailed meso-scale ply modelling of composites, incorporating Continuum Damage Mechanics (CDM) to account for intraply behaviour, encompassing fibre and matrix damage, and the Cohesive Zone Model (CZM) to capture interply behaviour such as delaminations. A slightly different approach to the aforementioned methods is the research conducted by Bouvet et al. [8]. Instead of employing CDM, they adopt a Discrete Fracture Method (DFM) that represents delaminations and matrix cracking through cohesive interface elements. Moreover, in [8], they also consider the effects of permanent indentation in the modelling approach and used ply aligned meshing. Building upon this foundation, Hongkarnjanakul et al. [12] extended and validated this approach for various layup

* Corresponding author at: Delft University of Technology, Faculty of Aerospace Engineering, Kluyverweg 1, 2629 HS Delft, The Netherlands.
E-mail address: N.vanHoorn@tudelft.nl (N. van Hoorn).

https://doi.org/10.1016/j.compstruct.2024.118726
Received 11 April 2024; Received in revised form 21 October 2024; Accepted 18 November 2024
Available online 26 November 2024

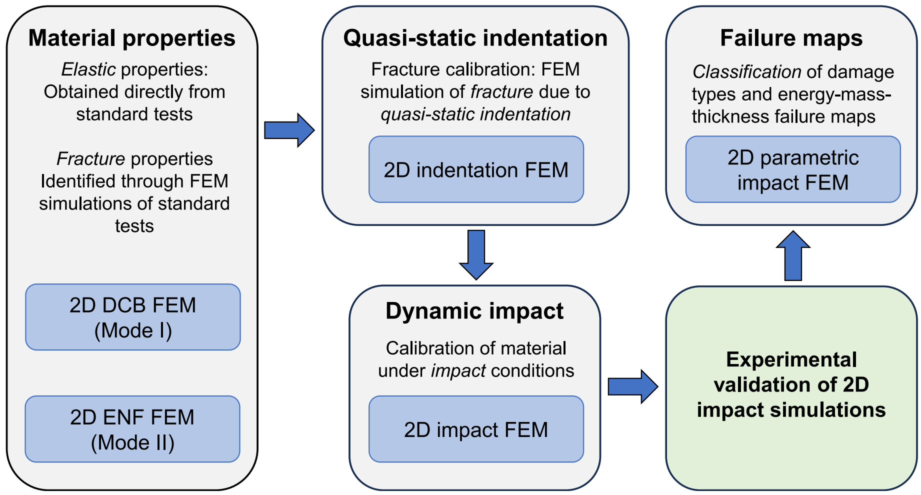

Fig. 1. Flowchart of the methodology.

configurations. Furthermore, Rivallant et al. [13] adopted a similar modelling strategy to incorporate Compression After Impact (CAI).

Performing these detailed ply-by-ply high-fidelity modelling demands a substantial computational effort to ensure converged results. This trade-off between accuracy and efficiency presents a significant challenge, even for conventional thin composite laminates. However, this challenge is amplified when dealing with thick composite laminates, where the modelling must include a substantial number of plies, typically ranging from 60 to 120. Examples of these thick composite laminates are found in highly loaded aerospace structures, such as wing root sections, landing gear components, and lugs [14]. The behaviour of these structures subjected to impact is not fully understood and research that focuses on modelling impact in thick composite laminates is limited. Gama and Gillespie [15] analysed 13.2 mm thick glass fibre reinforced laminates subjected to impacts ranging from low-velocity to ballistic. Farooq and Myler [16] studied 7.4 mm thick CFRP laminates. Both of these studies encountered shared challenges in modelling impacts, including limitations related to mesh size, the influence of strain rate effects, and uncertainties surrounding material properties. Sachse et al. [17] conducted a comprehensive investigation involving both experimental and numerical analyses of the impact and Compression After Impact (CAI) behaviour of CFRP laminates with thicknesses up to 12 mm. In their analysis of interlaminar damage, they employed the CZM and evaluated several different models. Among these models, the one that incorporated friction, accounted for strain rate effects, considered crack surface characteristics (e.g., saw tooth pattern), and incorporated cohesive strength reduction after delamination initiation demonstrated the closest alignment with experimental results. This study underscores the intricacy involved in modelling impact events and the numerous numerical and physical parameters essential for achieving detailed predictions.

Despite the significant work done in this field, the computational effort of current high-fidelity methods is still too high for practical applications, especially for thick composite structures. There is a need for an efficient methodology that can predict the impact behaviour and resulting damage for a wide range of impact cases, which is the focus of this work. The originality of this work lies partly in its application to thick composite structures, but primarily in the establishment of links between different modelling steps and a proposed impact methodology that is validated for a wide range of impact cases. This multi-step methodology enables consistent calibration and validation of damage due to impact. The consistent use of the DFM to extract data from experiments (i.e., fracture tests, indentation tests) assures consistency of the model parameters used in the simulations for impact. In addition, the modelling method includes a novel approach to consistently delete a partially failed cohesive element while accounting for the proper energy dissipation due to fracture. Due to its efficiency, the simulation framework enables the generation of novel failure maps including the thickness of a composite plate to elucidate the influence that this parameter has on damage under various impact conditions. For example, the analysis reveals that the ratio between ply delamination and ply matrix cracking due to impact has a non-monotonic behaviour with respect to impact energy and thickness, with the highest matrix damage observed for intermediate laminate thicknesses and impact energies.

The approach presented in this work takes a step-by-step path as illustrated in Fig. 1, beginning with *coupon modelling*, progressing to *quasi-static indentation*, and finally addressing *dynamic impact* events. An axi-symmetric two-dimensional (2D) modelling approach is employed, utilising a DFM with the CZM to account for both interlaminar (delaminations) and intralaminar (fibre/matrix) damage. To ensure fidelity in the representations, fabric waviness is incorporated to accurately capture the fracture surface and introduce plasticity in the bulk material to consider permanent indentation. Each step undergoes validation through comparison with experimental results including experimental data provided in previous work [18] for validating the simulations of dynamic impact in thick composites.

2. Numerical simulation of damage under quasi-static and impact conditions

This section outlines the steps taken to develop a numerical impact model for predicting fracture in thick laminated composite specimens. The developed methodology is employed for the analysis of two distinct models: the quasi-static indentation model and the dynamic impact model. Throughout the description, notable differences between these models are emphasised. A summary of each model, including the approximate number of Degrees of Freedom (DOF) and approximate user time, is provided in Table 1. The computations were performed on a compute cluster equipped with Intel Xeon Gold 6148 processors.

A 3D impact problem is defined of which the dimensions and boundary conditions (i.e., clamping and support) are based on the ASTM D7136 standard [19]. The impact problem is then formulated as a two-dimensional (2D) approximation. In this study, an axi-symmetric approach has been selected, as illustrated in Fig. 2. In this illustration the rotational symmetry is around the y-axis. This approach meets the requirement to model through-the-thickness damage, and the primary advantage is that the impactor is modelled accurately (i.e., spherical). However, a limitation of this approach is that the material properties are uniform in the circumferential direction around the axis of symmetry, while orthotropic materials have directional properties that vary

Table 1
Details of the models used for this study.

FEM model	Figure	2D assumption	Solver	DOF	User time [h]
DCB	3(a)	Plane stress	Abaqus/Implicit	74k	2.3
ENF	3(b)	Plane stress	Abaqus/Implicit	47k	3.9
Indentation	6	Axi-symmetric	Abaqus/Implicit	52k	27.5–66.1
Impact	2	Axi-symmetric	Abaqus/Explicit	200k–400k	8.0–26.6

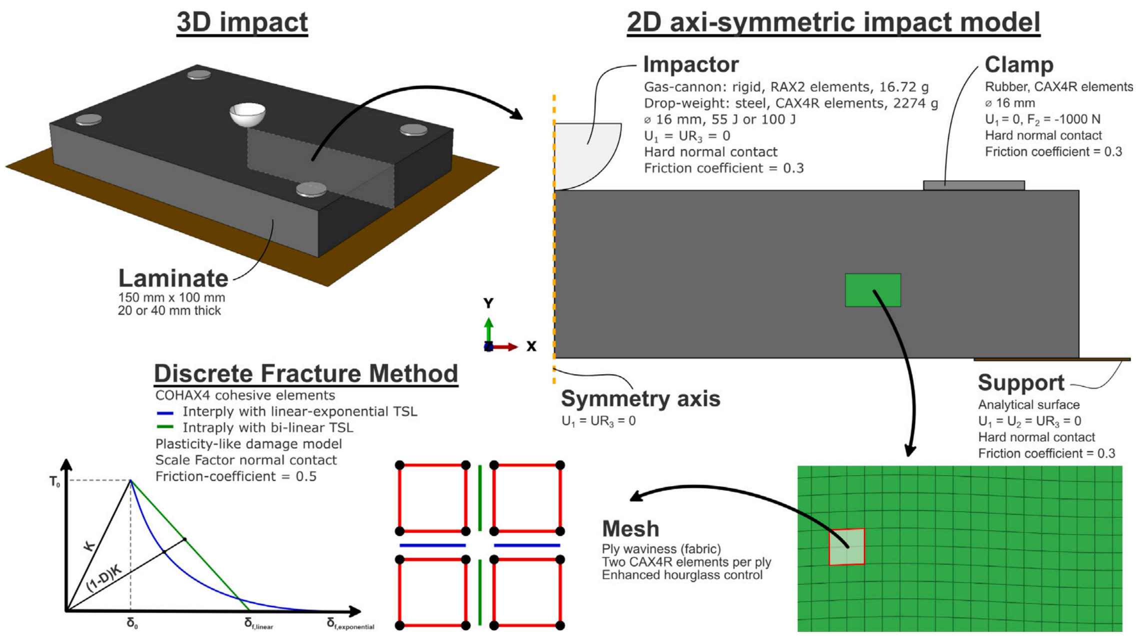

Fig. 2. Overview of the methodology where the 3D impact problem is represented with an 2D axi-symmetric impact model. A DFM with cohesive interface elements for inter- and intralaminar failure is used to predict impact damage.

with respect to the material coordinate system. Although a plane-stress or plane-strain 2D model would address this issue, the cylindrical representation of the impactor is deemed to be of greater importance. To mitigate the aforementioned modelling limitations, two model variants are created for each prediction, one in the xy-plane and one in the yz-plane. By using two different cross-sections, the material's behaviour is captured more accurately by accounting for the directional properties in two orthogonal directions.

To accurately capture localised fracture phenomena, a DFM incorporating cohesive interface elements is utilised. This method accounts for both interply (e.g., delaminations) and intraply (e.g., matrix/fibre failure) fractures. By employing the DFM instead of smeared fracture methods, a more realistic representation of fracture behaviour could be achieved, for instance in scenarios involving complex crack patterns resulting from the propagation of multiple individual cracks. An additional advantage of employing the DFM is the ability to directly quantify and compare results with experimental data, facilitating insights into crack lengths and energy dissipation.

The FEM analysis is conducted using the Abaqus software package. Leveraging the integration of Python within Abaqus, the pre-processing stage is entirely scripted, enabling parameterisation and seamless integration of cohesive interface elements. Additionally, Python is employed for post-processing and data analysis tasks. The discretisation of the model employs linear axi-symmetric quadrilateral elements with reduced integration (CAX4R) for the bulk material and the impactor in case of large-mass low-velocity impact. For the dynamic impact model applied to small-mass high-velocity impacts a rigid impactor with RAX2 elements is used. Within the laminate, cohesive interface elements (COHAX4) are inserted between all bulk elements. The mesh size is set to half the ply thickness, as for this mesh size convergence was found for certain damage mechanisms, notably the permanent dent depth. Furthermore, it was observed that the global response in terms of force and displacement exhibited negligible sensitivity to the mesh sizes investigated. To account for the waviness of fabric materials, the meshing is adjusted accordingly, as will be explained in Section 3.

During impact, permanent dents are observed in the area below the impactor. These dents have been ascribed to different damage mechanisms, including the accumulation of debris, but effectively behave similar to plastic deformations in other materials such as metals, hence existing plastic models are sometimes used to reproduce this effect. Correspondingly, damage-induced permanent dents in impact simulations have been phenomenologically described using plasticity-like models [8,20]. A similar modelling approach is adopted in the present work where a strain rate-independent anisotropic plasticity model is incorporated in the constitutive model assigned to the bulk elements. For the present study, von Mises yield criterion is used and the subsequent hardening is calibrated using the quasi-static indentation model and experimental data. Each ply has a separately assigned von Mises plasticity model with a distinct hardening behaviour that is assigned according to the fibre orientation in the ply. This modelling approach allows to effectively incorporate an anisotropic plastic behaviour for the composite material. In particular, the response in the local transverse direction (perpendicular to the fibres) reflects the plastic-like behaviour ascribed to matrix cracking debris whereas the response in the fibre direction is assumed to be mostly elastic until failure. The purpose of using a plasticity model for the damage-induced dents is that a damage model alone is not equipped to reproduce permanent deformations. It is important to notice that the plasticity-like damage model is only relevant in the region adjacent to the impact where debris is anticipated. The damage in the rest of the specimen, connected to cracking without debris, is captured using the DFM.

The material behaviour of cohesive elements is described by a Traction–Separation Law (TSL). In this study, a linear-exponential TSL is applied for interply fracture, as illustrated in Fig. 2. A bi-linear TSL is used for intraply fracture. Preliminary comparisons showed that these softening laws captured the observed behaviour more accurately. This was in line with what several authors have reported in the past [8, 20]. The initial slope of the TSL resembles the penalty stiffness K_{11}, proposed by Turon et al. [21] as follows:

$$K_{11} = \frac{aE_{33}}{t_{\text{ply}}}. \tag{1}$$

Here, E_{33} is the through-the-thickness elastic modulus of the sub-laminate, and t_{ply} is the ply thickness of the sub-laminate. The coefficient a is taken as 50, which, according to Turon et al. [21], typically results in a stiffness loss due to the interface of only about 2%. The peak of the TSL represents the cohesive strength (i.e., normal fracture strength T_N or tangential fracture strength T_S), and this value is determined from out-of-plane tension and interlaminar shear strength experiments. After reaching the cohesive strength, the stiffness is decreased exponentially as a function of the damage variable D. When the cohesive element completely fails (i.e., it reaches maximum degradation with $D = D_{\text{max}}$), it is deleted. The mode-mixity is characterised by a Benzeggagh–Kenane law with a power (i.e., BKP) of 1.75 for a brittle epoxy resin [22]. According to Turon et al. [23], the shear interface stiffness (K_{22} and K_{33}) should be adjusted to improve the accuracy using the following relation:

$$K_{22} = K_{33} = K_{11}\left(\frac{G_{Ic}}{G_{IIc}}\right)\left(\frac{T_S}{T_N}\right)^2, \tag{2}$$

where G_{Ic} and G_{IIc} are, respectively, the mode I and mode II fracture energies (i.e., fracture toughness) per unit cracked area.

To enhance numerical stability, it may be beneficial to establish a maximum degradation D_{max} that is less than 1. This approach mitigates convergence problems with otherwise partially damaged elements that can only transmit relatively low cohesive tractions. However, using a cut-off value D_{max} less than 1, the dissipated energy is lower than the specified fracture energy because the cohesive elements are deleted prematurely. Therefore, to ensure that the correct amount of energy is dissipated upon early failure, a modified fracture energy is used such that the energy dissipated at the cut-off value coincides with the actual fracture energy of the material. The modified expression is further explained in Appendix A.

After the failure of cohesive elements in the model, a contact definition is required between the remaining bulk elements. In addition, a contact definition was established between the impactor and the first few plies. Both definitions utilise hard normal contact with the penalty enforcement method and separation after contact is allowed. In the tangential direction penalty friction is used with isotropic directionality and no dependencies. For the dynamic impact simulations a more strict normal behaviour is selected, as will be explained in Section 4. A friction coefficient of 0.3 was used for contact between the impactor and the specimen, while a higher coefficient of 0.5 was used inside the laminate. These friction coefficients were calibrated and also adjusted with values reported in the literature (see. e.g., [24]).

3. Material parameters: quasi-static calibration and validation

The Double-Cantilever Beam (DCB) and End-Notched Flexure (ENF) tests are two well-established experiments used to experimentally determine the material fracture properties. These properties are used as input in the traction–separation laws that are assigned to cohesive interface elements in FEM models. Simulations of the actual DCB and ENF tests are conducted to calibrate the fracture properties and also to verify the numerical implementation. After this, the methodology is applied to a separate class of tests, namely quasi-static indentation experiments, to check if the correct damage mechanisms are accounted for, which serves as a validation step for the overall numerical procedure.

3.1. Simulation of DCB and ENF experiments

The mode I interlaminar fracture energy per unit cracked area (i.e., G_{Ic}) can be obtained from a DCB test, while an ENF test is used to determine the mode II interlaminar fracture energy per unit cracked area (i.e., G_{IIc}). The material system used for these tests is identical to the one used for validation in Section 5, and further details are given in that section.

The DCB specimen measures 297 × 25 mm and has a $[0_8]$ layup, resulting in a thickness of 2.5 mm. An artificial delamination is introduced in the middle of the laminate using a Teflon film with an overlap of 63 mm. Each specimen is loaded until the delamination initiates, then unloaded and reloaded until a final crack length of approximately 100 mm is reached. As the initiation load and failure behaviour differs for each specimen, there may be slight differences in the loading cycle. After the DCB testing, the cracked specimen is reused for the ENF experiment by cutting the end to leave a 35 mm starter crack.

Details of the DCB and ENF model can be found in Fig. 3. The DCB and ENF experiments are simulated in Abaqus/Standard to verify the implementation of interlaminar cohesive elements. At the same time, the elastic behaviour is verified by comparing the initial slope of the simulations and the experiments. Experimental results from coupon tests are used for the material inputs. The model consists of two sub-laminates of four plies each that are connected using interlaminar cohesive elements. The artificial delamination of 63 mm is modelled by removing cohesive elements. Between the two sub-laminates, contact is defined with a friction coefficient of 0.5. For the bulk material plane stress elements (CPS4R) are used with second-order accuracy and enhanced hourglass control.

The experimental data and the results of finite element numerical simulations based on traction–separation laws and cohesive elements are compared to closed-form expressions obtained from beam theory in combination with the Irwin-Kies relation (i.e., the compliance method that uses a relation between the fracture energy and the change in compliance due to crack growth). In the closed-form expressions, the load applied, F, as a function of crack length, a, for DCB is described by the following formula [25]:

$$F(a) = \sqrt{\frac{G_{Ic} w^2 h^3 E_{11}}{96a^2}}, \tag{3}$$

where w is the specimen width, h is the specimen height, and E_{11} is the longitudinal modulus of elasticity. Similarly, for ENF, this closed-form function, as described in [26], is given as

$$F(a) = \sqrt{\frac{2G_{IIc} w^2 h^3 E_{11}}{9a^2}}. \tag{4}$$

In Fig. 4, the numerical prediction is compared with a single experiment and the expression from the compliance method given in (3). The predicted initial slope is in perfect alignment with the experiment, which provides confidence in the elastic behaviour of the laminate. However, there is a slight discrepancy between the slope at reloading due to differences in initial crack length after the pre-load between the experiment and prediction. During crack propagation, the numerical prediction closely follows the expression (3) from the compliance method and is in line with the experiment. The predicted fracture energy is within 1% of the input G_{Ic}, which can be further improved by increasing the mesh density.

For ENF simulations, it was observed that the inclusion of waviness is crucial for capturing the correct failure behaviour during the crack propagation phase. In fabric materials, delaminations typically follow the yarns that exhibit undulations, which are dictated by the weave pattern [27]. In the numerical model, a sine wave pattern is incorporated into the mesh to account for this phenomenon. The amplitude of the sine wave (10% of the ply thickness) and its wavelength (12 times the ply thickness) are estimated based on visual inspection of

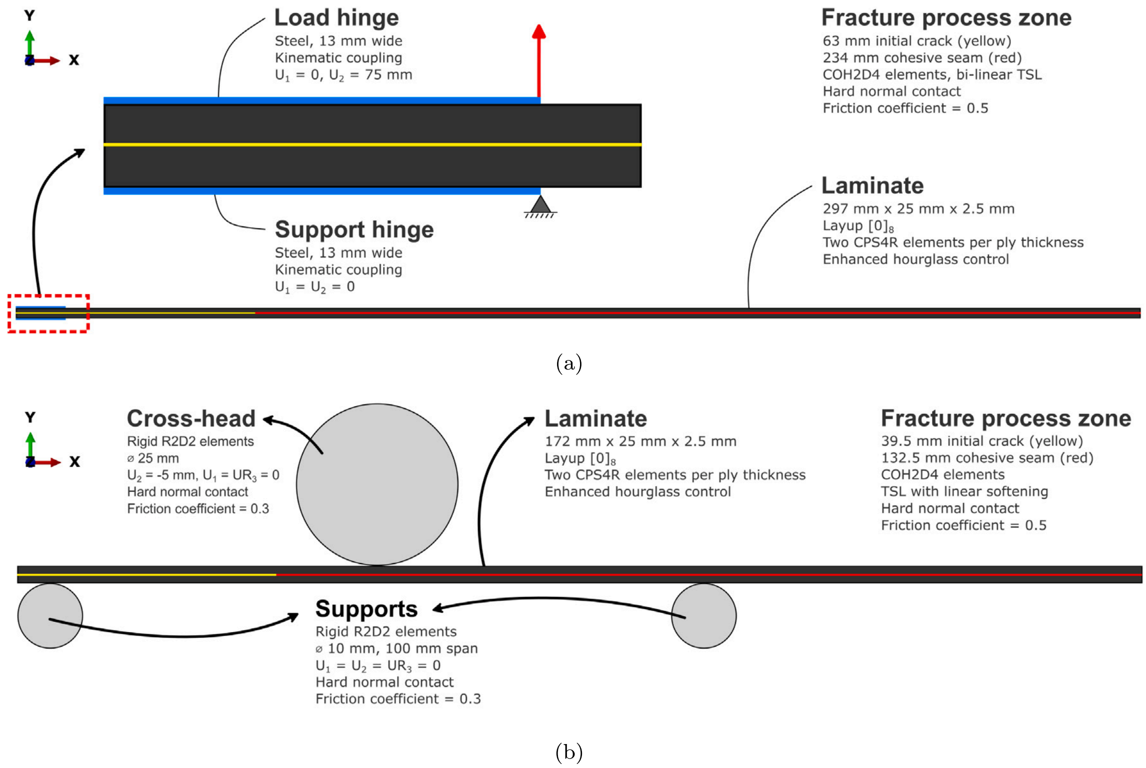

Fig. 3. Illustration of the models used for the identification of interlaminar fracture properties. (a) Double Cantilever Beam model for mode I and (b) End Notch Flexure model for mode II.

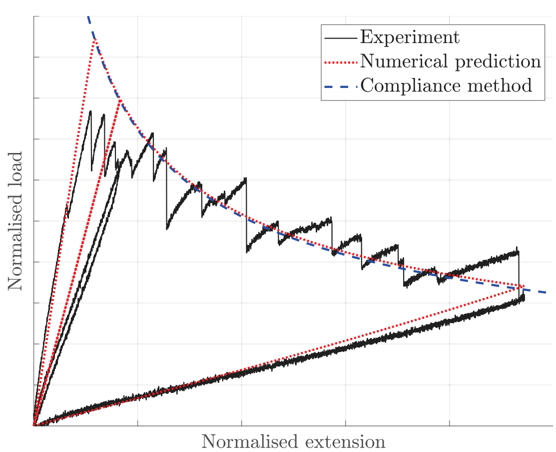

Fig. 4. Numerical prediction of one DCB test and comparison with the expression (3) (compliance method). The load and extension have been normalised by using a reference value.

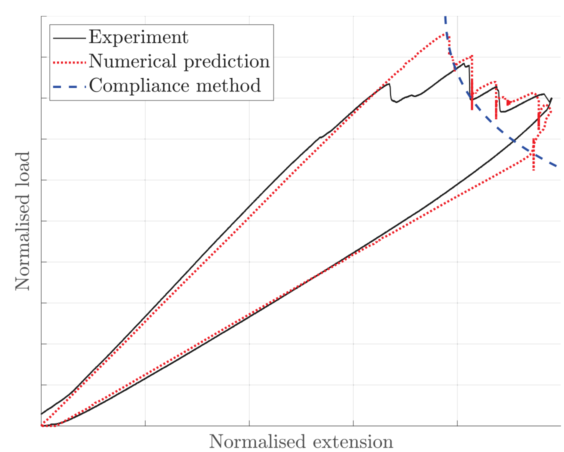

Fig. 5. Numerical prediction of one ENF test and comparison with the expression (4) (compliance method). The load and extension have been normalised by using a reference value.

cross-section cuts under a microscope. A sensitivity analysis reveals that the sine amplitude should be at least 5% to produce a noticeable effect. However, increasing the amplitude beyond this threshold does not significantly modify the results. On the other hand, the wavelength significantly influences the outcome, highlighting the importance of characterising it accurately.

The value of G_{IIc}, as derived from the ASTM standard that uses the ENF experiments, is re-calibrated by increasing it by 40% for the traction–separation relations used in the finite element model to better predict the overall behaviour of the same ENF experiments. Although these two values should nominally be the same, it is worth pointing out that they are obtained from two distinct methods (i.e., the ASTM standard relies on the compliance method, whereas the matching values from the finite element simulations are connected to the traction–separation relations that govern the cohesive elements in the simulations). An extensive study about this discrepancy falls outside of the scope of the present work, but the value of G_{IIc} used in all simulations is the one obtained from the FEM calibration of the experimental data.

It is also worth highlighting that the matching prediction was not only achieved by re-calibrating the tangential fracture energy G_{IIc} but also by including waviness, as demonstrated in Fig. 5. The discrete load drop events during crack propagation (i.e., the near vertical portions of the curve), could be traced back to the waviness during the simulations. The initial slope of the predicted curve is also consistent

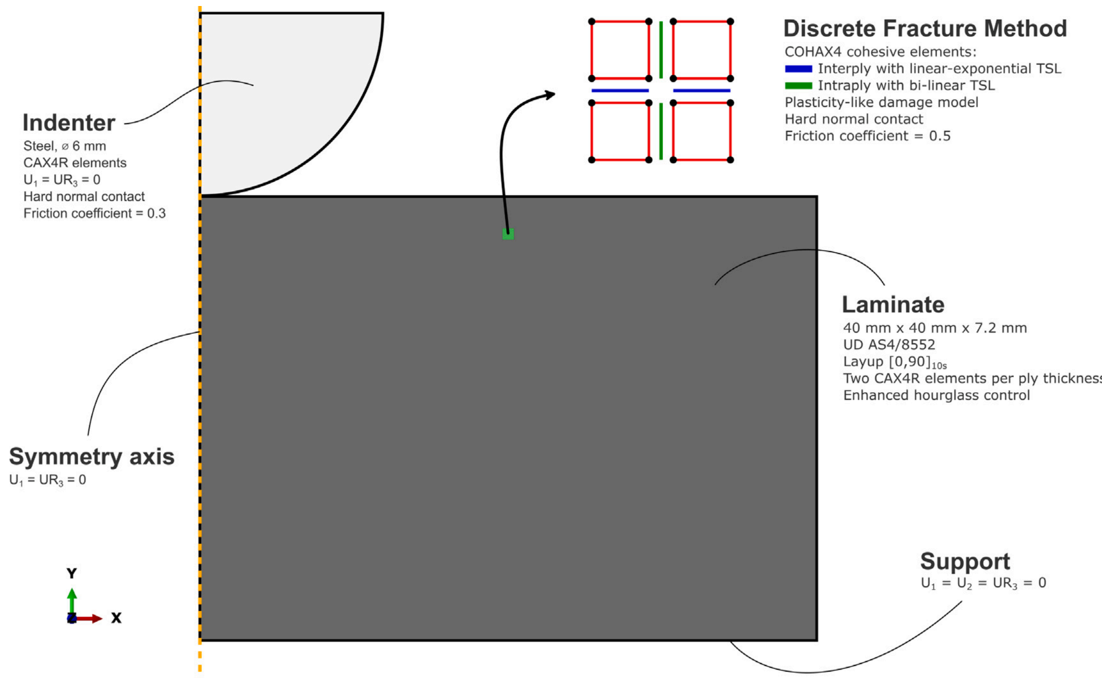

Fig. 6. Illustration of the quasi-static indentation model used for calibration of the DFM.

Table 2
Material properties used for the numerical analysis of quasi-static indentation experiments [7,28].

AS4/8552					Steel indenter-impactor	
E_{11} [GPa]	E_{22} [GPa]	G_{12} [GPa]	ν_{12} –	t_{ply} [mm]	E_{steel} [GPa]	ν_{steel} –
137.8	8.58	4.92	0.32	0.18	200	0.3
Interply and 90° intraply cohesives						
$T_{N,0}$ [MPa]	$T_{S,0}$ [MPa]	G_{Ic} [J/m^2]	G_{IIc} [J/m^2]	K_{11}	K_{22}	BKP
66.1	105.2	280	1106	2.86E16	1.83E16	1.75
0° intraply cohesives						
$T_{N,0}$ [MPa]	$T_{S,0}$ [MPa]	G_{Ic} [J/m^2]	G_{IIc} [J/m^2]	K_{11}	K_{22}	BKP
2042.1	408.4	20 000	800	2.86E16	2.86E16	1.75

with the experimental results, which further strengthens the reliability of the selected elastic properties. Moreover, the unloading slope also agrees with the experiments, which is equally significant and provides further justification for the choice of the fracture properties used in the simulation.

3.2. Simulation of quasi-static indentation experiments

In this section, quasi-static indentation experiments on thick composites are simulated using the DCB and ENF numerical models as a basis. An axi-symmetric 2D assumption is used and the DFM is implemented in the mesh (see Fig. 6). These quasi-static indentation simulations serve as a solid foundation for an impact model and include nearly all the necessary features for predicting impact damage.

The cohesive normal strength, denoted as $T_{N,0}$, has been determined through coupon tension tests, while the cohesive shear strength, represented as $T_{S,0}$, is assumed to be five times lower than the cohesive normal strength based on test results obtained by Chiem and Liu [29]. For modelling the longitudinal fibre fracture within the 0° plies, the intraply cohesive elements have been assigned a normal fracture energy of 20 kJ/m^2, as previously reported by Raimondo et al. [7]. In the case of intraply cohesive elements simulating matrix cracking within other plies, identical properties have been assigned to them as those of the interply cohesive elements (see Table 2).

The quasi-static indentation model is validated by comparing it to experiments conducted by Talagani [28]. In these experiments, square specimens measuring 40 × 40 mm, with a total thickness of 7.2 mm (equivalent to 40 plies), were used. The specimens were constructed using AS4/8552 Uni-Directional (UD) prepreg material, and the material properties are indicated in Table 2. For indentation, a spherical steel indenter with a radius of 3 mm was employed. The load was applied in a displacement-controlled manner through several steps: (1) 1.0 mm loading, (2) 0.5 mm unloading, (3) 0.5 mm reloading, and (4) 1.0 mm unloading. This loading cycle was applied in the numerical model, with a minor adjustment to account for an initial setup phase. The specimens were fully supported by a flat steel plate during the experiments such that no bending could occur.

The predicted force-indentation relationship is presented in Figs. 7(a)–7(d), showing that the calibration process has yielded accurate results. As previously mentioned, the model has two variants in the xy- and yz-planes, corresponding to $[0, 90]$ and $[90, 0]$ layups. The predicted cross-sectional damage of these two variants is compared to the experimental results of Talagani [28], as illustrated in Figs. 7(e) and 7(f). Although slight differences exist due to the orientation of the first layer, all damage mechanisms are captured and the predicted dimensions are accurate. Similar results were obtained for a Quasi-Isotropic (QI) layup, as verified through additional validation tests.

To analyse the effect of uncertainties in the model parameters that are difficult to measure, a sensitivity analysis was performed on the interply and intraply friction coefficient, the yield stress, the exponent of the exponential softening, the normal fracture energy, and cohesive shear strength factor with normal strength. The influence of these parameters on the peak force was investigated and the results are summarised in Table 3. The change refers to a deviation from the baseline value and the effect refers to the relative change in the peak force, categorised in three levels of influence as indicated in the caption (negligible, moderate and high). The interply friction coefficient was found to be relevant (i.e., moderate effect), with a higher coefficient

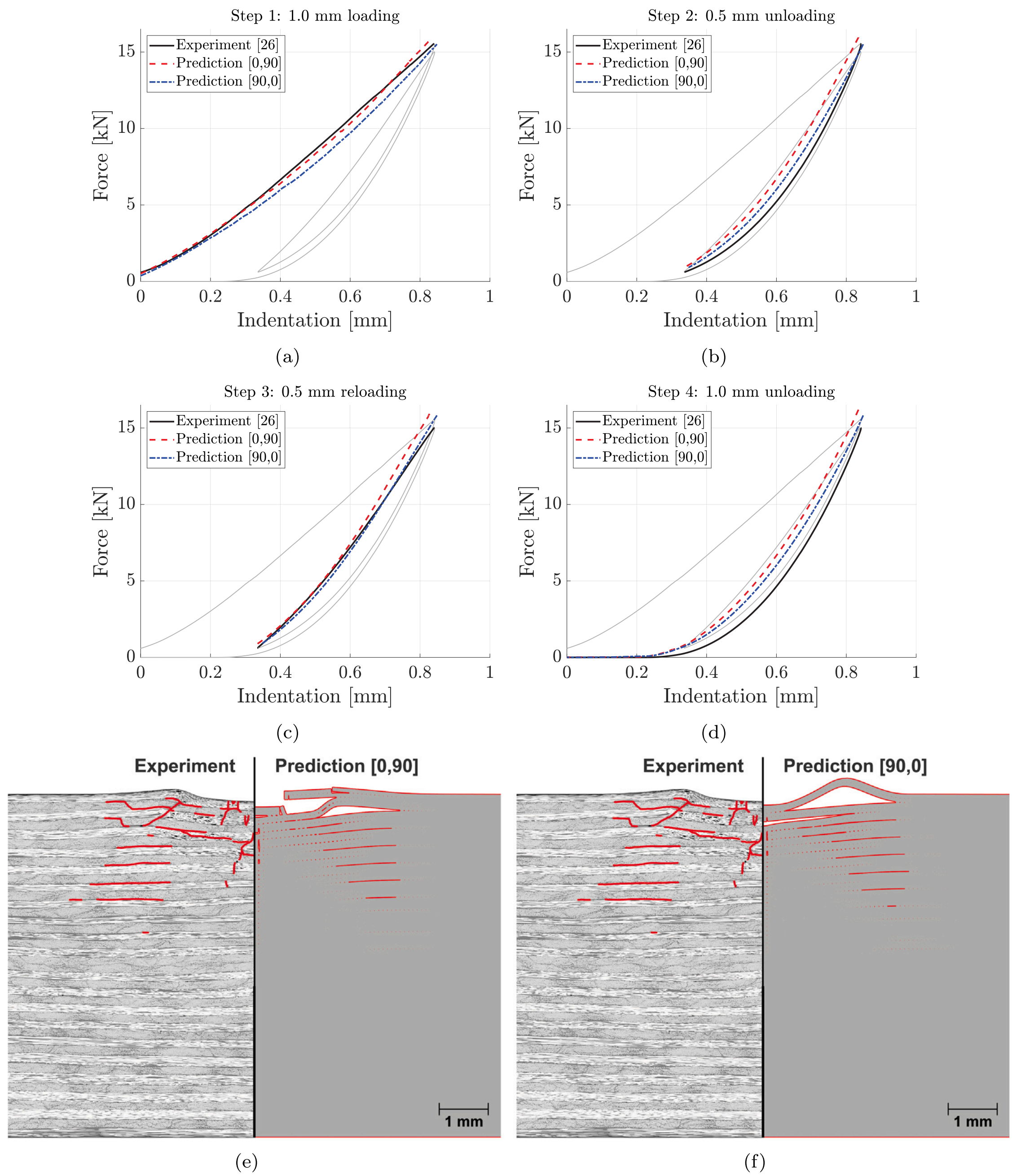

Fig. 7. Validation of the quasi-static indentation model by comparing with indentation experiments [28]. Two model variants are evaluated, with a [0, 90] and [90, 0] layup. (a-d) force-indentation prediction of each step in the loading history, (e) and (f) comparison of the predicted damage of the two model variants with cross-sectional cuts.

resulting in an increased peak force and reduced damage depth. While the intraply friction coefficient showed negligible influence on the damage dimensions, a lower value increased the amount of intraply damage. The value used for the yield stress was assumed equal to the compressive strength of the material and had a moderate effect on the results. Increasing the yield stress by 50% led to less than 10% increase in peak force and minimal effect on the resulting damage. The exponent of the exponential softening behaviour of cohesive elements had a negligible influence on the force history, while slightly affecting the resulting damage. The normal fracture energy of cohesive elements inside the 0° plies was based on literature and had a negligible influence on the force history, but increasing this value led to decreasing intraply damage. The shear factor sensitivity was found to be negligible on both the peak force and resulting damage.

Table 3
Effect of the calibrated parameters on the peak force predicted by the quasi-static indentation simulations. Negligible: < 0.05%/%, Moderate: 0.05-0.2%/%, High: > 0.2%/%.

Variable	Change	Effect
Interply friction coefficient	−50%	Moderate
Intraply friction coefficient	−50%	Negligible
Yield stress	−50%	Moderate
Exponential softening exponent	−50%	Negligible
Normal fracture energy	+100%	Negligible
Cohesive shear strength factor	−50%	Negligible

4. Material parameters: dynamic calibration

4.1. Calibration of interaction with impactor: contact and vibration

Although the 2D quasi-static indentation model can accurately predict damage under quasi-static conditions, the ultimate goal is to extend its capabilities to enable dynamic impact simulations. To achieve this, the model is converted to Abaqus/Explicit, which is a computationally efficient framework for impact problems. The frame used in the impact experiments for validation in Section 5 has a 125 × 75 mm cut-out, and the specimen is clamped at four points instead of being fully supported. Although this alternative representation can result in minimal bending of the thick specimens, its effect is considered negligible.

The impact forces in dynamic indentation experiments are much higher than those in quasi-static indentation experiments, making the contact definition between the plies critical in preventing penetration of bulk elements after cohesive element deletion. To address this issue, the hard contact definition used in the quasi-static indentation model was modified to a scale factor normal contact definition with a overclosure measure equal to the ply thickness divided by 125 and a contact stiffness factor of two. These properties were determined through a sensitivity study using a simplified model of two bulk elements connected with a single cohesive element and compressed. The objective was to minimise penetration with minimal increase in computational effort. Compared to the hard contact definition, the modified contact definition reduced penetration by 67% while increasing computational effort by only 72%.

In a dynamic simulation, stress waves generated by the impact will travel through the specimen, and it is essential to accurately define the interaction of these stress waves with cohesive elements. In particular, intact cohesive elements should not interfere with the stress wave, while a fully failed cohesive element should reflect the stress wave. To achieve this, it is necessary to ensure that the cohesive stiffness is high enough, as defined by (1). Ideally, the cohesive element should also have a near-zero density ρ_{coh}. However, reducing the density too much can significantly increase the computational time since the stable time increment δt is a function of $\sqrt{\rho_{coh}}$. Therefore, a density factor of 10^{-6} with respect to the bulk density is chosen to ensure correct interaction with stress waves while maintaining acceptable computational time.

During drop-weight impact tests, oscillations in the force readings were observed, which are more pronounced for impacts on thick composite specimens. These oscillations are linked to the eigenfrequencies of the drop-weight, and the frequency is a function of the thickness and geometry of the specimen. An experimental frequency analysis showed three axial eigenfrequencies at around 7000, 12000, and 13000 Hz. At the start of impact, the impact force is in either the 12000 or 13000 Hz eigenfrequency, and after impact, the drop-weight shows axial oscillations with approximately 7000 Hz. It is possible that the vibrating drop-weight during impact could affect the damage creation, so for numerical simulations of drop-weight impacts, the impactor is modelled in full.

4.2. Calibration of material properties under impact conditions

Rectangular specimens measuring approximately 140 × 100 mm with a 72 ply laminate and a total thickness of around 15 mm were utilised for the experiments. The material system used was a combination of HexForce T300 plain weave and HexFlow RTM6, and its elastic and strength properties were characterised with quasi-static tests. The dynamic impact tests were carried out using a 2.268 kg drop-weight impactor on nine specimens, with impacts at three different energy levels: 50, 72, and 98 J. The force–displacement history was recorded during each drop-weight impact. Additionally, some specimens were subjected to impacts with a 16.72 g bullet fired using a gas-cannon, with impact energies of 55 and 97 J. To quantify the damage resulting from the impacts, cross-section cuts of the specimens were inspected.

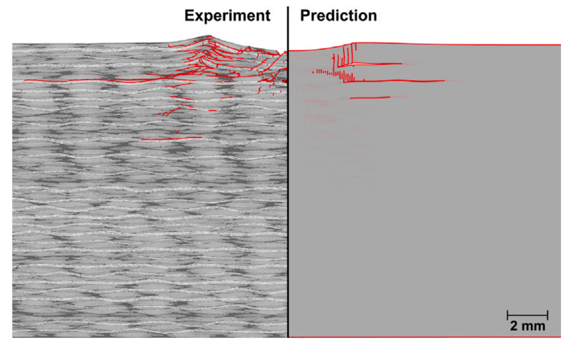

Fig. 8. Predicted damage of the 2D dynamic impact model compared to a cross-section cut of a 14.7 mm thick specimen that was subjected to a 50 J drop-weight impact.

Simulation of the drop-weight impact tests showed an accurate prediction of the global impact response. This indicates that the overall stiffness and dynamic effects are appropriately captured by the simulation. However, when comparing the numerically predicted damage patterns to the cross-section cuts, it was found that the predicted damage was significantly higher.

The discrepancy between the predicted and experimental results for the impact tests was ascribed to strain rate effects that are not present in the quasi-static setting used to calibrate the material and model parameters. The strain rate dependency of material properties is a common issue in dynamic impact simulations of composite materials [17,30–33]. It is known that for thermoset composites, these effects can be significant. Experimental investigations have shown varying results regarding the effect of strain rate depending on the material system used. In this work, the strain rate dependence of the material used for validation in Section 5 could not be fully characterised experimentally as this requires extensive testing under different strain rates. To address this issue, instead of using an explicit strain-rate dependent model, the effect of the model parameters in the rate-independent model previously developed were systematically analysed. In particular, the interlaminar cohesive strength was (re-)calibrated to compensate for strain rate effects, while other properties remained as calibrated for quasi-static tests. The experimental impact data of the tests mentioned above were used to calibrate the model for impact. The best overall result was achieved by increasing the interlaminar cohesive strength by a factor of two. This factor is consistent with IM7/8552 characterisations for impact simulations performed by Cui et al. [32,34].

Fig. 8 presents the predicted damage for the 50 J drop-weight impact with the re-calibrated interlaminar cohesive strength. All damage mechanisms are captured by the 2D numerical impact model. It should be noted that the accuracy of the predicted damage width and depth varies. This issue becomes apparent for cases where a significant dent is created, particularly for high-energy drop-weight impacts, which is not fully captured by the simplified 2D numerical impact model. However, for low-energy drop-weight impacts and gas-cannon impacts, the predicted damage is reasonably accurate in the sense that it is validated against experimental results. This can be illustrated by the following cases: For the 55 J gas-cannon impact, the damage depth is approximately 3 mm, while for the 97 J impact, it caused full through-thickness damage (i.e., 15 mm), and both cases are captured by the numerical model. Overall, these comparisons demonstrate that the modelling approach for quasi-static indentation is applicable for dynamic impact predictions with an appropriate accounting of strain rate effects, which can be achieved by calibrating the interlaminar cohesive strength.

5. Experimental validation of impact simulations

In Section 4, a 2D numerical impact model was developed and calibrated with 15 mm thick specimens. Most of the material parameters were calibrated with quasi-static tests as indicated in Section 3,

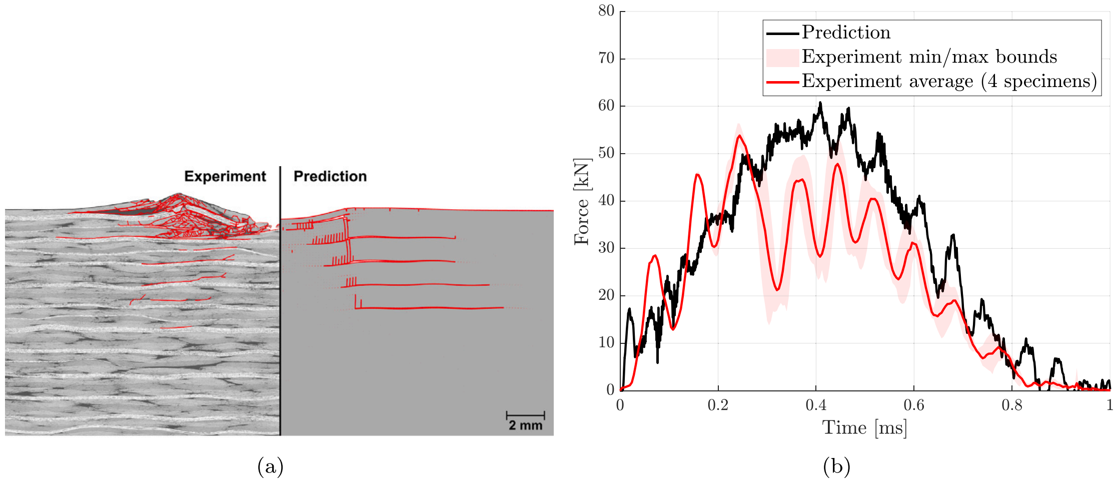

Fig. 9. Predicted damage of the 2D dynamic impact model compared to: (a) a cross-section cut of a 40 mm thick specimen that was subjected to a 55 J impact and (b) the average force history measured during the impact test of four specimens. Note: in (a) only the top 12 mm of the specimen is shown.

Table 4
Derived homogenised 3D elastic ply properties of the quasi-UD 2/2 twill weave fabric used for validation.

E_{11} [GPa]	E_{22} [GPa]	E_{33} [GPa]	G_{12} [GPa]	G_{13} [GPa]	G_{23} [GPa]	ν_{12} [–]	ν_{13} [–]	ν_{23} [–]	t_{ply} [mm]
126.5	28.3	9.0	4.1	3.9	2.7	0.06	0.36	0.49	0.3109

while the impact case required calibration of the contact interaction with the impactor and accounting for strain rate effects. With this set of parameters, the model is further validated by comparing the predictions with a separate (independent) set of experiments as previously reported in [27]. The impact experiments involved the use of 20 mm and 40 mm thick specimens produced with a 2/2 twill weave fabric and Resin Transfer Moulding (RTM) with properties listed in Table 4. Both Quasi-Isotropic (QI) $[-45/0/45/90]_{ns}$ and OrthoTropic (OT) $[[-45/0/45/90_2/-45/45/90_2]_3/-45/45/90_2/0]_s$ layups were used for the 20 mm specimens. Low-velocity drop-weight and high-velocity gas-cannon impacts were performed at 55 and 100 J, resulting in a total of 10 different impact cases for validation, with four specimens for each impact case. The force and displacement history were recorded, and for gas-cannon impacts, a novel procedure was used to derive these from high-speed camera images. After impact, dent depth was measured, and the delaminated area (i.e., width, height, depth) was obtained using C-scans. For each impact case, one specimen was used for cross-section analysis, while the other three were employed for compression-after-impact tests.

As part of the validation of the large-mass cases, a Fourier analysis was conducted to compare the eigenfrequencies predicted by the numerical model with the experimental data. During loading, the predicted eigenfrequencies matched well with the experimental results. During unloading, a distinct eigenfrequency of 13500 Hz was observed in the numerical model, which is consistent with the impactor eigenfrequency found in Section 4. However, this specific eigenfrequency was not clearly observed in the experimental data during impact testing.

The validation criteria can be categorised into two groups: *impact response* and *damage characteristics*. The former includes peak force, maximum impactor displacement, and return velocity, which are indicators of whether the global behaviour is accurately predicted. The latter includes dent depth, damage width/height, and damage depth, which are measures of damage characteristics. To illustrate the range of predictions the cases for the best and least accurate results in terms of predicted damage and impact response are presented here. For both cases the predicted cross-sectional damage is compared with a cross-section cut of one of the specimens. In this comparison, it should be noted that the predicted cross-sectional damage is based on the axi-symmetric model with a radius of 125 mm (i.e., the average of the width and height). Conversely, the experimental cross-section cut is taken along the width of the specimen. While the damage for these thick specimens is localised and relatively circular due to limited bending, a similar cross-section cut along the height of the specimen might reveal a different damage pattern.

The 55 J drop-weight impact on the 40 mm thick specimen with a QI layup had a reasonably accurate predicted impact response. The peak force was over-predicted by 27% (see Fig. 9(b)) while the maximum impactor displacement was predicted with an error of −4%. However, the return velocity was significantly over-predicted by a factor of two. These results were representative of most drop-weight impacts. The higher peak force was due to the limited dent creation in the numerical model. Even though the maximum impactor displacement was similar, the absence of dent creation resulted in higher specimen deflection, leading to a higher predicted return velocity. Overall, the dent depth was under-predicted by 39% for this case. The overall delaminated area in terms of width and height was predicted at 24.5 mm, which was only 6% lower than the 26 mm measured with C-scans and well within the experimental scatter. The predicted damage depth of 5.4 mm was 31% over-predicted compared to the C-scan. However, the cross-section in Fig. 9(a) showed a damage depth of 6.5 mm, indicating that for this specimen some delaminations were not captured by the C-scan.

The 100 J gas-cannon impact on the 20 mm thick specimen with a QI layup showed significant over-prediction of damage, as seen in Fig. 10. Here the predicted damage extends through the full thickness, which is not in accordance with the experimental results. The peak force of gas-cannon impacts was generally significantly over-predicted by more than 50%. The high-speed images showed that the first few layers evaporated at high-energy gas-cannon impacts, and this was not captured by the numerical model. As a result, a higher peak force was generated, initiating stress waves that led to delaminations. Consequently, the specimen deflection was higher, causing the propagation of delaminations throughout the full thickness, resulting in an almost zero return velocity.

Despite the case shown in Fig. 10, in general the simulations show that the model can predict the general damage mechanisms, such as fibre- and matrix cracking interacting with delaminations. As a result, the model is quite capable of predicting the overall damage state and global force and displacement histories for the 10 impact cases with a reasonable agreement. Despite over and under-predicting some specific quantities, the model is in reasonable agreement with for the majority of impact cases in terms of the global damage, which is particularly noteworthy given the minimal computational effort required

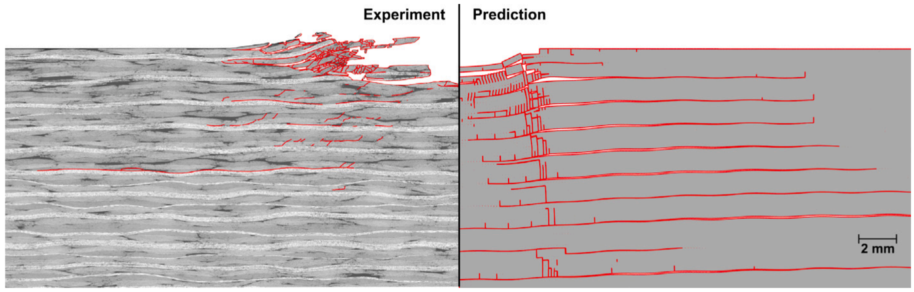

Fig. 10. Predicted damage of the 2D dynamic impact model compared to a cross-section cut of a 20 mm thick specimen that was subjected to a 100 J impact. Note: only the top 13 mm of the specimen is shown and the predicted damage extends through the full thickness.

by this simplified 2D model. For instance, the reference 3D impact model of a 40 mm thick specimen would require approximately 26 million DOF (typical element size 0.3 mm), resulting in a computational time of more than 17 days (using 32 CPUs). In contrast, the axi-symmetric 2D model, under nominally similar simulation conditions and software/hardware resources, has approximately 0.4 million DOF (typical element size 0.15 mm), requires only 8 h of computational time (using 24 CPUs), representing an improvement of more than a factor of 50. The computational efficiency of the axi-symmetric 2D model enables comparison of different laminates. However, its accuracy should be carefully evaluated with experiments or a representative three-dimensional simulation to ensure its applicability for different cases.

6. Impact failure maps in composites: effect of impact energy, impact mass, and laminate thickness

As an application of the simulation methodology for impact, a parametric analysis was conducted to establish general trends of damage under various impact conditions. Using the 2D numerical impact model, a total of 84 simulations were conducted with varying impact energy (i.e., 5–150 J), laminate thickness (5–30 mm), and impact mass (20, 200, and 2000 g). For the generation, submission, and post-processing PYTHON scripting was used. To minimise the computational time, the total impact duration was estimated by using a semi-analytical impact response model developed by the authors [18]. From the simulation results, several key parameters were extracted, including the total damage width, coefficient of restitution, total crack energy, and interply/intraply energy ratio. To present the results in a comprehensive way, failure maps were created by plotting the aforementioned parameters against the impact energy and laminate thickness, with a separate plot for each impact mass. These global impact indicators were chosen since the simulation methodology was able to predict them reasonable well during the validation step. The failure maps provide a visual representation of the damage evolution and help to identify the critical impact conditions that lead to failure of the laminates.

6.1. Failure map: damage width

In the context of this study, the total damage width in carbon fibre composite materials is a critical factor that affects the mechanical properties and integrity of the material. It directly relates to the delaminated area which is commonly used when quantifying impact damage. The extent of damage can significantly impact the material's stiffness, strength, and fatigue life. Therefore, accurately predicting the total damage width is vital for ensuring the reliability and safety of the structure.

The failure map for damage width is presented in Fig. 11. The results indicate that higher impact energies lead to increased damage width, as expected, and that thinner laminates result in greater damage width. Furthermore, the damage width is found to be greater for smaller mass impacts, and in the case of a 20 g impactor, the slope is steeper, suggesting that the laminate thickness has a slightly lesser effect. These findings may be attributed to the dynamic effects that occur at higher impact velocities.

6.2. Failure map: coefficient of restitution

The coefficient of restitution is a fundamental parameter in impact analysis, used to quantify the elasticity of two colliding objects by the ratio between the relative velocity after collision and relative velocity before collision (i.e., impact velocity). In composite materials, the coefficient of restitution plays a crucial role in determining the damage mechanisms and failure modes of the structure under impact. For example, a higher coefficient of restitution may result in a more localised damage pattern, with less delamination and fibre fracture. On the other hand, a lower coefficient of restitution may lead to a more extensive damage region, with more matrix cracking and delamination. Furthermore, the coefficient of restitution can be used to optimise the design of composite structures for impact resistance, by selecting materials with specific elastic properties that minimise the energy absorbed during impact.

Analysis of the failure map in Fig. 12 reveals distinct differences between small-mass, high-velocity impacts, and larger impact masses. The coefficient of restitution appears to be relatively constant for all impact energies and laminate thicknesses in the former case, whereas for the latter case, a coefficient of restitution of zero is observed at high impact energies on thin laminates, indicating complete laminate penetration. Conversely, at low impact energies on thick laminates, nearly all energy is returned to the impactor, resulting in a coefficient of restitution near one. This region corresponds to a small damage width, as illustrated in Fig. 11. These results suggest a correlation between the coefficient of restitution and damage width for larger impact masses.

6.3. Failure map: total crack energy

In impact analysis, the total crack energy is a crucial parameter as it quantifies the energy used to initiate and propagate cracks within a composite material. The total crack energy is directly linked to the amount of energy absorbed during impact and the extent of damage within the composite material. For the failure maps, the crack energy was determined by analysing every cohesive element throughout its complete loading history. As the loading history generally comprises both normal and shear opening, the energy dissipated in both mode I and II fractures have been monitored and added together.

The results from Fig. 13 show a distinct peak in total crack energy at 150 J impact energy for a 20 mm thick specimen, particularly for the small-mass impact case of 20 g. Thinner specimens exhibit damage that extends through the full thickness, but the amount of material damaged is relatively small, resulting in lower total crack energy. For specimens with a thickness of 20 mm, the damage still extends through the full thickness. However, for thicknesses above this, the damage is contained in the upper region of the specimen, leading to a decrease in total crack energy. While the damage width slightly increases for

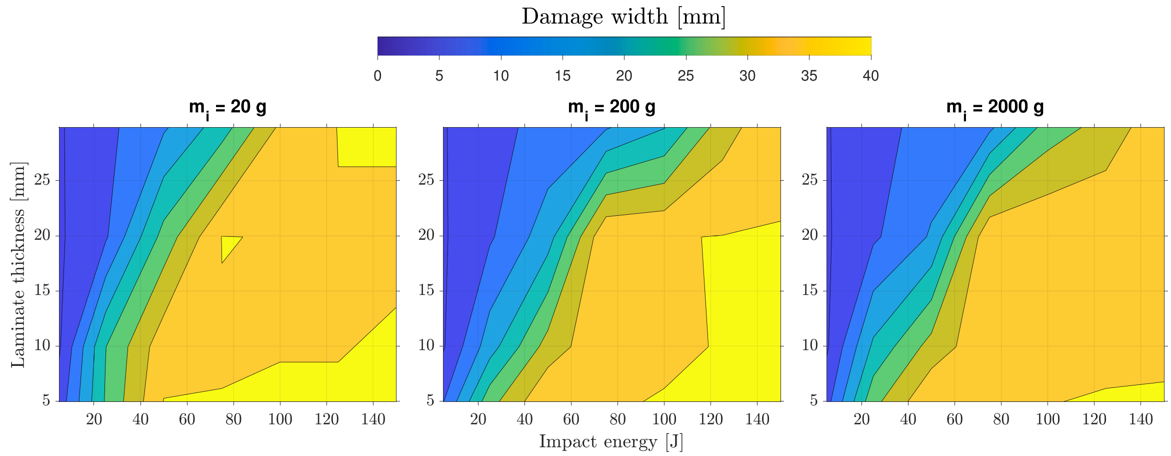

Fig. 11. Damage width as a function of impact energy, laminate thickness, and impact mass.

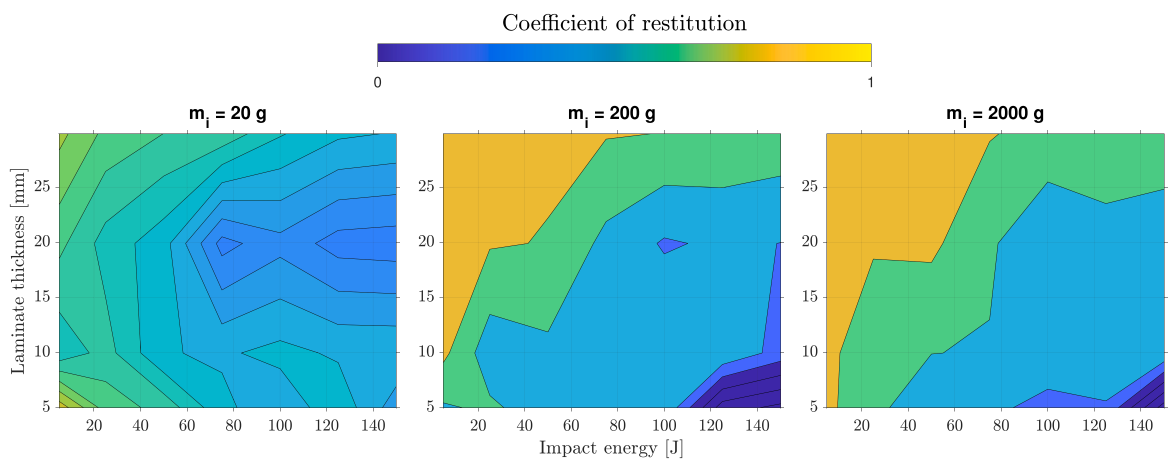

Fig. 12. Coefficient of restitution (i.e., ratio of impact velocity and return velocity) as a function of impact energy, laminate thickness, and impact mass.

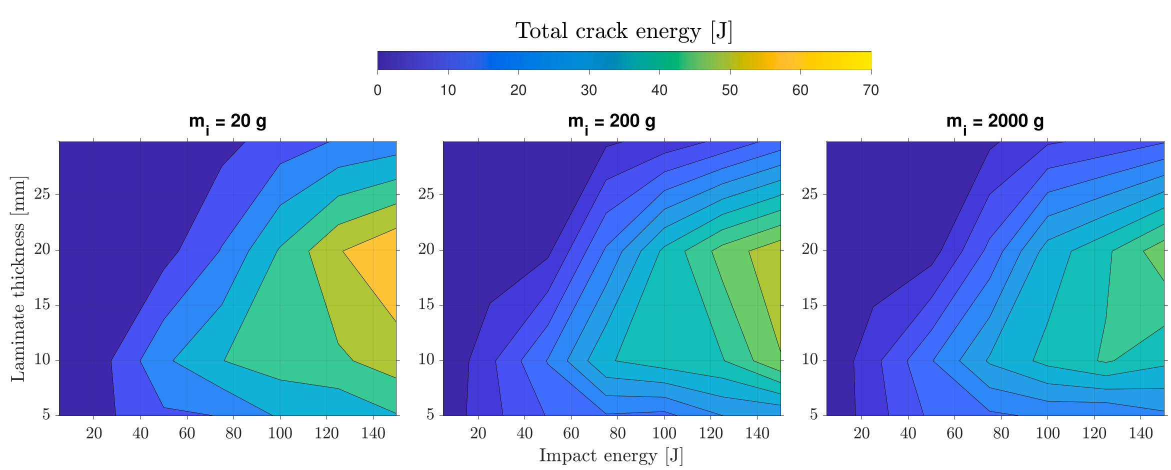

Fig. 13. Total crack energy (i.e., all energy going into cohesive damage) as a function of impact energy, laminate thickness, and impact mass.

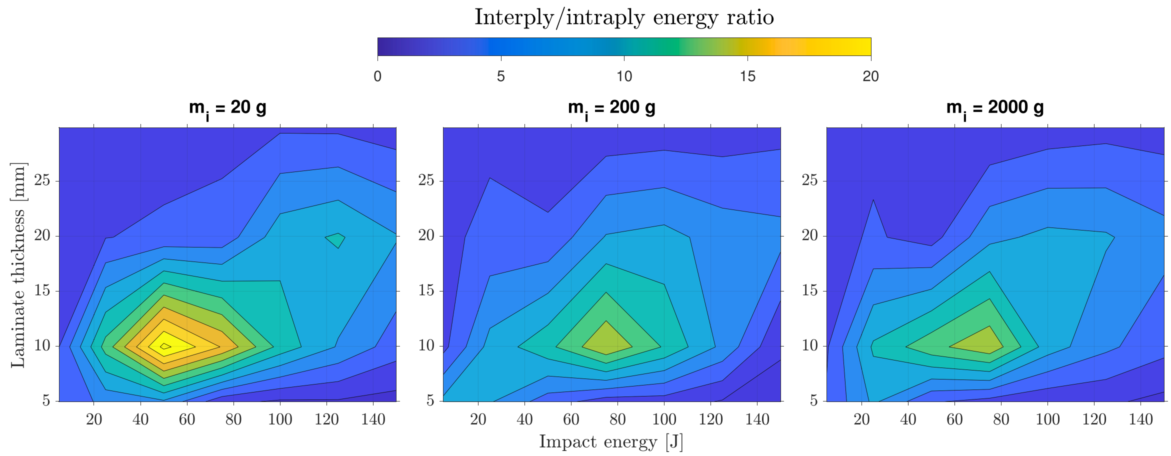

Fig. 14. Ratio between energy going into delaminations (i.e., interply) and fibre/matrix cracking (i.e., intraply) as a function of impact energy, laminate thickness, and impact mass.

thicker specimens, as observed in Fig. 11, the damage depth remains constant. This observation may prove useful in the design of composite structures.

6.4. Failure map: interply/intraply energy ratio

In composite materials, the interply crack energy represents the energy required to initiate and propagate a crack between two adjacent layers (i.e., delamination), while the intraply crack energy represents the energy required to initiate and propagate a crack within a single layer of the composite material. The ratio of interply to intraply crack energy can provide valuable insights into the failure mechanisms and crack propagation behaviour within the composite material. Both the occurrence of delaminations and fibre/matrix damage are important factors that influence the residual strength of the composite after impact.

The resulting failure map is shown in Fig. 14. The interply/intraply energy ratio shows a non-monotonic behaviour, with the highest interply energy observed for intermediate laminate thicknesses and impact energies. This suggests that the delamination damage mechanism is more dominant in these cases, while the intraply damage mechanism becomes more significant at higher impact energies and thinner laminates, or at lower impact energies for thicker laminates. This is behaviour most evident for small-mass high-velocity impacts.

The effect of the interply/intraply ratio on the residual strength after impact is of interest. A high ratio indicates mainly delamination, which has limited effect on tensile performance, but significantly affects the residual strength in compression due to sub-laminate buckling. Conversely, a low ratio indicates significant fibre/matrix damage, reducing the effective cross-sectional area of the composite, resulting in a substantial decline in tensile strength, accompanied by a comparatively smaller reduction in compressive strength. The results in Fig. 14 show that thicker specimens (> 20 mm) exhibit fewer delaminations and should therefore experience less of a reduction in compressive strength. This behaviour is observed during compression after impact tests performed by van Hoorn et al. [27], where a 55 J small-mass impact reduces the compressive strength by 11.9% for a 20 mm thick specimen and only 8.8% for a 40 mm thick specimen.

7. Conclusions

This work presents a methodology for simulating the impact behaviour of thick fabric CFRP composite laminates using a DFM approach with cohesive interface elements for interlaminar and intralaminar damage. The methodology was developed through a step-by-step calibration, verification, and validation process:

1. Calibration and verification of numerical cohesive behaviour by comparison with DCB and ENF experiments under quasi-static conditions. Including fabric waviness and calibrating the mode II fracture energy (G_{IIc}) from TSL-based ENF simulations provided a more suitable value than using the compliance method.
2. Simulation of quasi-static indentation tests to validate the material and numerical properties used. These simulations captured all relevant failure mechanisms for impact on thick composite laminates.
3. Modification of the 2D quasi-static indentation model to dynamic impact loading and transition to an explicit solver.
    a. Optimisation of normal contact definitions between plies to account for high impact forces.
    b. Adjustment of stiffness and density of cohesive elements to accurately represent stress waves.
    c. Modelling of the entire impactor for drop-weight impact tests to consider eigenfrequencies and oscillations in the contact force.
4. Calibration experiments to account for strain rate effects of the material, resulting in the determination that doubling the interlaminar cohesive strength provides satisfactory results.
5. Validation of the methodology through comparisons with impact experiments covering a range of low- and high-velocity impacts with varying impact energy, layup, and laminate thickness.

The 2D modelling approach with axi-symmetric elements was found to accurately predict the overall damage state and global force and displacement histories for most impact cases. Despite its limitations, the 2D modelling approach offers a key advantage: manageable computational effort. To evaluate this, 84 impact simulations were conducted to generate failure maps. These maps enabled the assessment of how impact energy, mass, and laminate thickness affect the damage width, coefficient of restitution, total crack energy, and the interply/intraply energy ratio. Some general trends were observed:

- For thick composite laminates the damage width is smaller and damage is primarily concentrated in the upper region of the laminate.
- A correlation was found between damage width and coefficient of restitution for larger impact masses.
- Thicker laminates yield a higher coefficient of restitution, indicating more energy is returned to the impactor, resulting in a narrower in-plane damage and lower total crack energy.
- A high interply/intraply energy ratio was found for intermediate laminate thicknesses and impact energies, indicating prevalence of delaminations.

- For thicker laminates subjected to low impact energies, the interply/intraply energy ratio decreased, indicating fewer delaminations.
- The reduced extent and depth of damage in thick laminates is beneficial for compression after impact strength.
- The increased compression after impact strength (as a fraction of pristine strength) in thicker laminates compared to thinner laminates can aid in formulating criteria and certification approaches that no longer require Barely Visible Impact Damage (BVID).

CRediT authorship contribution statement

Niels van Hoorn: Writing – review & editing, Writing – original draft, Visualization, Validation, Software, Methodology, Investigation, Formal analysis, Conceptualization. **Sergio Turteltaub:** Writing – review & editing, Supervision, Methodology, Conceptualization. **Christos Kassapoglou:** Writing – review & editing, Supervision, Methodology, Conceptualization. **Wouter van den Brink:** Writing – review & editing, Supervision, Conceptualization.

Declaration of Generative AI and AI-assisted technologies in the writing process

During the preparation of this work the author(s) used ChatGPT in order to improve the scientific writing. After using this tool/service, the author(s) reviewed and edited the content as needed and take(s) full responsibility for the content of the publication.

Declaration of competing interest

The author(s) declared no potential conflicts of interest with respect to the research, authorship, and/or publication of this article.

Acknowledgment

The author(s) disclosed receipt of the following financial support for the research, authorship, and/or publication of this article: This work is part of a PhD research program supported by the Royal Netherlands Aerospace Centre in collaboration with Delft University of Technology.

Appendix A. Adjusted traction–separation-law accounting for early element deletion

A Traction–Separation Law (TSL) used in conventional cohesive elements relates constitutively the cohesive traction τ transmitted through the cohesive surface and the corresponding crack opening displacement δ, for both normal and shear openings. This constitutive information is commonly prescribed either using a potential-based formulation or specifying component-wise relations. For compactness, the relations in this appendix are shown for a pure mode (I, II or III), which simplifies the presentation. The TSL can be characterised by its cohesive stiffness K (a numerical parameter) and the fracture properties of the material, namely the fracture strength τ_0 and the fracture energy G. The TSL also requires an expression for the degradation relation (i.e., the shape of the TSL for increasing values of a damage variable D). Two types of degradation relations are considered in this appendix, namely linear and exponential softening. Furthermore, for all types of degradation relations, the *elastic* crack opening or closing of the cohesive surface is conventionally modelled with a linear relation $\tau = (1-D)K\delta$, where the degradation parameter D ranges nominally from $D = 0$ (no damage) to $D = 1$ (complete damage).

As outlined above, the maximum degradation $D_{\max}$ is nominally equal to 1 for all TSLs. However, in practice it can be calibrated to remove cohesive elements before they reach final failure (i.e., $D_{\max} < 1$). Typically, using a value of $D_{\max}$ smaller than 1 can be advantageous for computational efficiency in explicit solvers. However, it is important to note that the total energy dissipated when an element is prematurely removed is lower than the fracture energy G used as input. This appendix outlines the procedure for compensating for this missing fracture energy for both linear and exponential softening.

A.1. Adjusted linear TSL with $D_{max} < 1$

The crack opening displacement δ_0 at initiation of damage can be obtained from the undamaged linear elastic loading relation, i.e.,

$$\delta_0 = \frac{\tau_0}{K} \, . \tag{A.1}$$

In a linear softening TSL, the cohesive traction τ is a linearly decreasing function of the current crack opening displacement δ, namely

$$\tau(\delta) = \tau_0 \left(1 - \frac{\delta - \delta_0}{\delta_f - \delta_0}\right) , \quad \delta_0 \le \delta \le \delta_f \tag{A.2}$$

where δ_f is the crack opening displacement at failure. For $\delta \ge \delta_f$, then $\tau(\delta) = 0$. In the case of linear degradation (softening), the fracture energy G is obtained by computing the work required to completely degrade the cohesive surface (per unit area), i.e., in view of (A.1), (A.2),

$$G = \int_0^{\delta_f} \tau(\delta)\mathrm{d}\delta = \frac{\tau_0 \delta_f}{2} \, ,$$

hence the crack opening displacement at failure δ_f is related to the fracture energy and the fracture strength as

$$\delta_f = \frac{2G}{\tau_0} = \frac{2G}{K\delta_0} \, , \tag{A.3}$$

where the second expression is obtained using (A.1) again.

In the scenario where the maximum degradation is less than one, the cohesive element is removed at a crack opening displacement equal to δ_{cutoff}, which is less than the original value δ_f. To account for this discrepancy, an adjusted TSL can be used that preserves the *same* fracture strength τ_0 as the original TSL, but with an *adjusted* fracture energy G^* and, therefore, with an adjusted crack opening displacement at failure δ_f^*. The cohesive traction of the adjusted TSL, denoted as τ^*, is also given by a linear degradation function of the crack opening displacement δ but using the adjusted parameters, i.e.,

$$\tau^*(\delta) = \tau_0 \left(1 - \frac{\delta - \delta_0}{\delta_f^* - \delta_0}\right) , \quad \delta_0 \le \delta \le \delta_f^* \, . \tag{A.4}$$

However, in practice the crack opening displacement δ does not reach the final value δ_f^* since the element is removed when the opening is equal to $\delta_{\mathrm{cutoff}} < \delta_f^*$. The adjusted fracture energy G^* is chosen such that the energy dissipated due to fracture up to $\delta = \delta_{\mathrm{cutoff}}$ coincides with the actual fracture energy of the material G, thereby accounting for the correct energy balance, including dissipation.

To determine the adjusted values, the first step is to compute the energy dissipated in the adjusted TSL that is not accounted for due to element deletion at the cutoff value by calculating the integral of (A.4) from δ_{cutoff} to δ_f^*, i.e.,

$$\tau_0 \int_{\delta_{\mathrm{cutoff}}}^{\delta_f^*} \left(1 - \frac{\delta - \delta_0}{\delta_f^* - \delta_0}\right) \mathrm{d}\delta = \tau_0 \frac{\left(\delta_f^* - \delta_{\mathrm{cutoff}}\right)^2}{2\left(\delta_f^* - \delta_0\right)} \, . \tag{A.5}$$

The adjusted fracture energy G^* should be equal to the actual fracture energy G plus the unaccounted energy dissipated given in (A.5), which, in view of (A.3), provides the following relation:

$$G^* = \frac{\delta_f^* \tau_0}{2} = \frac{\delta_f \tau_0}{2} + \tau_0 \frac{\left(\delta_f^* - \delta_{\mathrm{cutoff}}\right)^2}{2\left(\delta_f^* - \delta_0\right)} \, . \tag{A.6}$$

Solving for the adjusted crack opening displacement at failure δ_f^* gives

$$\delta_f^* = \frac{\delta_0 \delta_f - \delta_{\mathrm{cutoff}}^2}{\delta_0 + \delta_f - 2\delta_{\mathrm{cutoff}}} \, . \tag{A.7}$$

As in the original TSL, the adjusted cohesive traction τ^* can also be written as a function of the stiffness degradation D, i.e.,

$$\tau^*(\delta) = (1 - D)\, K\delta = \frac{\tau_0 (1 - D)}{\delta_0}\delta \, , \tag{A.8}$$

where the second relation is obtained using (A.1). Equating the cohesive traction as given separately by (A.4) and (A.8) when the cut-off

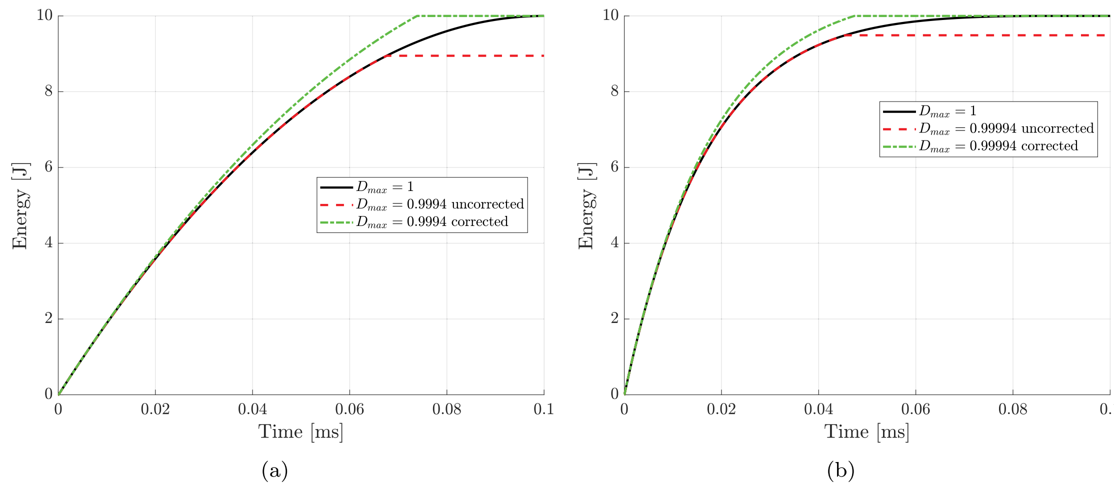

Fig. A.1. Verification of the modified Traction–Separation-Law accounting for early element deletion by single cohesive element tests in Abaqus for (a) linear softening with $D_{\max} = 0.9994$ and (b) exponential softening with $D_{\max} = 0.99994$.

state has been reached, i.e., when $D = D_{\max}$ and $\delta = \delta_{\text{cutoff}}$, provides the following relation:

$$\tau_0 \left(1 - \frac{\delta_{\text{cutoff}} - \delta_0}{\delta_f^* - \delta_0} \right) = \frac{\tau_0 \left(1 - D_{\max}\right)}{\delta_0} \delta_{\text{cutoff}} \,. \tag{A.9}$$

Solving this equation for δ_{cutoff} gives

$$\delta_{\text{cutoff}} = \frac{\delta_0 \delta_f^*}{\delta_f^* + D_{\max} \left(\delta_0 - \delta_f^* \right)} \,. \tag{A.10}$$

Substituting (A.10) in (A.7) and solving for δ_f^* gives the adjusted crack opening displacement at failure in terms of the chosen maximum stiffness degradation $D_{\max}$, i.e.,

$$\delta_f^* = \frac{\delta_0 D_{\max} \left(2\delta_f - \delta_0 D_{\max} + 2\delta_f D_{\max} + \sqrt{\delta_0} \sqrt{\delta_0 D_{\max}^2 - 4\delta_f D_{\max} + 4\delta_f} \right)}{2\left(1 - D_{\max}\right)\left(\delta_0 - \delta_f + (\delta_0 + \delta_f) D_{\max}\right)} \,, \tag{A.11}$$

hence, in view of (A.1) and (A.3), the adjusted linear TSL is now completely specified in terms of the material parameters (i.e., the fracture strength τ_0 and fracture energy G) as well as in terms of the chosen numerical simulation parameters (i.e., the cohesive stiffness K and the maximum degradation $D_{\max}$).

A.2. Adjusted linear-exponential TSL with $D_{max} < 1$

As in the previous case, the crack opening displacement δ_0 at initiation of damage is given by (A.1). After damage initiation, the subsequent degradation for an linear-exponential TSL is given by

$$\tau(\delta) = \tau_0 \left(1 - \frac{1 - e^{-\alpha(\delta - \delta_0)/(\delta_f - \delta_0)}}{1 - e^{-\alpha}} \right) \,, \quad \delta_0 \le \delta \le \delta_f \tag{A.12}$$

where α is a model parameter. For $\delta \ge \delta_f$, then $\tau(\delta) = 0$. This equation can alternatively be written as

$$\tau(\delta) = \tau_0 \left((1 + c)\, e^{-\alpha(\delta - \delta_0)/(\delta_f - \delta_0)} - c \right), \quad \delta_0 \le \delta \le \delta_f \,, \tag{A.13}$$

where the constant c is given by

$$c = \frac{1}{e^{\alpha} - 1} \,. \tag{A.14}$$

For the exponential softening case, a similar procedure can be followed as was shown for the linear softening case. However, there is no explicit solution in this case. Therefore, an iterative approach is followed. First, the fracture energy G can be related to the work required to completely degrade the cohesive surface, computed as the integral of τ from 0 to δ_0 without damage (work required to initiate the damage due to the artificial cohesive stiffness) and the integral of τ given in (A.13) from δ_0 to δ_f, i.e.,

$$G = \frac{\tau_0 \delta_0}{2} + \int_{\delta_0}^{\delta_f} \tau(\delta) \mathrm{d}\delta = \frac{\delta_0 \tau_0}{2} + \left(c - \frac{1}{\alpha} \right) \tau_0 (\delta_0 - \delta_f) \,. \tag{A.15}$$

Solving this equation for the crack opening displacement at failure δ_f results in

$$\delta_f = \frac{2\left(e^{\alpha} - 1\right) \alpha \frac{G}{\tau_0} - \left(e^{\alpha}(\alpha - 2) + \alpha + 2\right) \delta_0}{2\left(e^{\alpha} - \alpha - 1\right)} \,. \tag{A.16}$$

As in the case of linear degradation, the degradation parameter D ranges nominally from 0 to 1, but a maximum degradation value $D_{\max}$ less than 1 can be used to remove a cohesive element before final failure. Denote again as δ_{cutoff} the crack opening displacement when the degradation variable reaches the value $D_{\max}$. To properly account for the fracture energy when an element is prematurely removed, an adjusted traction–separation relation is used with the same strength τ_0 as the original TSL, but with an adjusted fracture energy G^* and therefore an adjusted crack opening displacement at failure δ_f^* such that the energy dissipated up to δ_{cutoff} is equal to the actual fracture energy G. Denoting as τ^* the traction of an adjusted TSL and evaluating (A.8) and (A.13) at δ_{cutoff} and $D = D_{\max}$ for an adjusted TSL, provides two separate expressions for τ^* at the cut-off point, which can be equated to each other, i.e.,

$$\tau_0 \left((1 + c)\, e^{-\alpha(\delta_{\text{cutoff}} - \delta_0)/(\delta_f^* - \delta_0)} - c \right) = \tau_0 \frac{\left(1 - D_{\max}\right)}{\delta_0} \delta_{\text{cutoff}} \,. \tag{A.17}$$

Solving this for δ_f^* gives

$$\delta_f^* = \delta_0 - \frac{\alpha \left(\delta_{\text{cutoff}} - \delta_0 \right)}{\log \left(\frac{c\delta_0 + \delta_{\text{cutoff}}(1 - D_{\max})}{(1 + c)\delta_0} \right)} \,. \tag{A.18}$$

Observe that in this case δ_f^* is given in terms of δ_{cutoff}, for which there is no closed-form expression. An iterative procedure is implemented to circumvent this issue. The objective is to ensure that the fracture energy dissipated up to δ_{cutoff} of the adjusted TSL matches the actual fracture energy value G of the material, i.e.,

$$G_{\text{cutoff}}^* = \int_0^{\delta_{\text{cutoff}}} \tau^*(\delta) \mathrm{d}\delta = G \,, \tag{A.19}$$

where, using the linear elastic loading part from 0 to δ_0 and the expression for $\tau^*(\delta)$ from δ_0 to δ_{cutoff} as given in (A.13) for the corresponding adjusted parameter δ_f^*, the term G_{cutoff}^* can be expressed as

$$G_{\text{cutoff}}^* = \frac{\delta_0 \tau_0}{2} - \tau_0 \frac{c + 1}{\alpha} \left(\delta_f^* - \delta_0 \right) \left(e^{-\alpha\left(\delta_{\text{cutoff}} - \delta_0\right)/\left(\delta_f^* - \delta_0\right)} - 1 \right) - \tau_0 c \left(\delta_{\text{cutoff}} - \delta_0 \right) \,. \tag{A.20}$$

To achieve this, an initial guess of δ_{cutoff} is continuously updated, and consequently, δ_f^* is also updated using (A.18) until the matching condition given by (A.19) and (A.20) is satisfied.

The above procedure has been verified through a simple single cohesive element test in Abaqus. Three cases were evaluated: (1) $D_{\max} = 1$, (2) with an unadjusted fracture energy, and (3) with an adjusted fracture energy. The results for both the linear (i.e., with $D_{\max} = 0.9994$) and exponential (i.e., with $D_{\max} = 0.99994$) cases are illustrated in Fig. A.1. The range of values for the damage variable D that correspond to significant cohesive degradation are typically clustered close to 1 since the cohesive damage scales as $(1-D)K$, with the cohesive stiffness given in (1), which should become comparable or smaller than the actual elastic stiffness E. Consequently, for an apparently high value of $D_{\max}$, a significant amount of fracture energy is unaccounted for in the unadjusted case.

Data availability

The data that has been used is confidential.

References

[1] Kassapoglou C. Design and analysis of composite structures. John Wiley & Sons, Ltd; 2010, http://dx.doi.org/10.2514/4.867804.

[2] Federal Aviation Administration. Advisory circular AC 20-107B. 2009, Available at https://www.faa.gov/.

[3] Esrail F, Kassapoglou C. An efficient approach for damage quantification in quasi-isotropic composite laminates under low speed impact. Composites B 2014;61:116–26, Elsevier BV..

[4] Massart PFR, Viswanath Dhanisetty VS, Kassapoglou C, Verhagen WJC, Curran R. Deducing the physical characteristics of an impactor from the resultant damage on aircraft structures. Int J Solids Struct 2020;200–201:94–105. http://dx.doi.org/10.1016/j.ijsolstr.2020.04.024.

[5] Donadon MV, Iannucci L, Falzon BG, Hodgkinson JM, de Almeida SFM. A progressive failure model for composite laminates subjected to low velocity impact damage. Comput Struct 2008;86:1232–52. http://dx.doi.org/10.1016/j.compstruc.2007.11.004.

[6] Tita V, de Carvalho J, Vandepitte D. Failure analysis of low velocity impact on thin composite laminates: Experimental and numerical approaches. Compos Struct 2008;83:413–28. http://dx.doi.org/10.1016/j.compstruct.2007.06.003.

[7] Raimondo L, Iannucci L, Robinson P, Curtis PT. A progressive failure model for mesh-size-independent FE analysis of composite laminates subject to low-velocity impact damage. Compos Sci Technol 2012;72:624–32. http://dx.doi.org/10.1016/j.compscitech.2012.01.007.

[8] Bouvet C, Rivallant S, Barrau JJ. Low velocity impact modeling in composite laminates capturing permanent indentation. Compos Sci Technol 2012;72:1977–88. http://dx.doi.org/10.1016/j.compscitech.2012.08.019.

[9] Sun XC, Hallett SR. Barely visible impact damage in scaled composite laminates: experiments and numerical simulations. Int J Impact Eng 2017;109:178–95. http://dx.doi.org/10.1016/j.ijimpeng.2017.06.008.

[10] Zhou J, Wen P, Wang S. Finite element analysis of a modified progressive damage model for composite laminates under low-velocity impact. Compos Struct 2019;225:111113. http://dx.doi.org/10.1016/j.compstruct.2019.111113.

[11] Falcó O, Lopes CS, Sommer DE, Thomson D, Ávila RL, Tijs BHAH. Experimental analysis and simulation of low-velocity impact damage of composite laminates. Compos Struct 2022;287:115278. http://dx.doi.org/10.1016/j.compstruct.2022.115278.

[12] Hongkarnjanakul N, Bouvet C, Rivallant S. Validation of low velocity impact modelling on different stacking sequences of CFRP laminates and influence of fibre failure. Compos Struct 2013;106:549–59. http://dx.doi.org/10.1016/j.compstruct.2013.07.008.

[13] Rivallant S, Bouvet C, Hongkarnjanakul N. Failure analysis of CFRP laminates subjected to compression after impact: FE simulation using discrete interface elements. Composites A 2013;55:83–93. http://dx.doi.org/10.1016/j.compositesa.2013.08.003.

[14] de Vries HPJ. Development of a main landing gear attachment fitting using composite material and resin transfer moulding. Techreport NLR-TP-2009-732, NLR - Netherlands Aerospace Centre; 2010.

[15] Gama BA, Gillespie Jr JW. Finite element modeling of impact, damage evolution and penetration of thick-section composites. Int J Impact Eng 2011;38:181–97. http://dx.doi.org/10.1016/j.ijimpeng.2010.11.001.

[16] Farooq U, Myler P. Finite element simulation of damage and failure predictions of relatively thick carbon fibre-reinforced laminated composite panels subjected to flat and round noses low velocity drop-weight impact. Thin-Walled Struct 2016;104:82–105. http://dx.doi.org/10.1016/j.tws.2016.03.011.

[17] Sachse R, Pickett AK, Middendorf P. Simulation of impact and residual strength of thick laminate composites. Composites B 2020;195:108070. http://dx.doi.org/10.1016/j.compositesb.2020.108070.

[18] van Hoorn N, Kassapoglou C, van den Brink WM. Impact response prediction and sensitivity analysis of thick laminated composite plates. Techreport NLR-TP-2019-529, NLR - Royal Netherlands Aerospace Centre; 2020.

[19] ASTM International. Standard test method for measuring the damage resistance of a fiber-reinforced polymer matrix composite to a drop-weight impact event. 2015, ASTM D7136/D7136M-15.

[20] Singh H, Mahajan P. Modeling damage induced plasticity for low velocity impact simulation of three dimensional fiber reinforced composite. Compos Struct 2015;131:290–303. http://dx.doi.org/10.1016/j.compstruct.2015.04.070.

[21] Turon A, Dávila CG, Camanho PP, Costa J. An engineering solution for mesh size effects in the simulation of delamination using cohesive zone models. Eng Fract Mech 2007;74:1665–82. http://dx.doi.org/10.1016/j.engfracmech.2006.08.025.

[22] Camanho PP, Dávila CG. Mixed-mode decohesion finite elements for the simulation of delamination in composite materials. Technical report NASA/TM-2002-211737, Hampton, VA 23681-2199: NASA Langley Research Center; 2002.

[23] Turon A, Camanho PP, Costa J, Renart J. Accurate simulation of delamination growth under mixed-mode loading using cohesive elements: definition of interlaminar strengths and elastic stiffness. Compos Struct 2010;92:1857–64. http://dx.doi.org/10.1016/j.compstruct.2010.01.012.

[24] Gerendt C, Dean A, Mahrholz T, Rolfes R. On the progressive failure simulation and experimental validation of fiber metal laminate bolted joints. Compos Struct 2019;229:111368. http://dx.doi.org/10.1016/j.compstruct.2019.111368.

[25] Standard test method for mode I interlaminar fracture toughness of unidirectional fiber-reinforced polymer matrix composites, (no. ASTM D5528-13). West Conshohocken, PA: ASTM International; 2013, http://dx.doi.org/10.1520/D5528-13.

[26] Standard test method for determination of the mode II interlaminar fracture toughness of unidirectional fiber-reinforced polymer matrix composites, (no. ASTM D7905/D7905M-14). West Conshohocken, PA: ASTM International; 2014, http://dx.doi.org/10.1520/D7905_D7905M-14.

[27] van Hoorn N, Kassapoglou C, Turteltaub SR, van den Brink WM. Experimental damage tolerance evaluation of thick fabric carbon/epoxy laminates under low-velocity and high-velocity impact and compression-after-impact. J Compos Mater 2022;56:761–78. http://dx.doi.org/10.1177/00219983211060501.

[28] Talagani MR. Impact analysis of composite structures Phd thesis, Delft University of Technology; 2014, URL: http://resolver.tudelft.nl/uuid:f576163e-3d28-4b76-b50e-2431622c1da5.

[29] Chiem C-Y, Liu Z-G. The relationship between tensile strength and shear strength in composite materials subjected to high strain rates. J. Eng. Mater. Technol. 1988;110:191–4. http://dx.doi.org/10.1115/1.3226030.

[30] Li X, Yan Y, Guo L, Xu C. Effect of strain rate on the mechanical properties of carbon/epoxy composites under quasi-static and dynamic loadings. Polym Test 2016;52:254–64. http://dx.doi.org/10.1016/j.polymertesting.2016.05.002.

[31] Van Blitterswyk J, Fletcher L, Pierron F. Characterisation of the interlaminar properties of composites at high strain rates: a review. Adv Exp Mech 2017;2:3–28. http://dx.doi.org/10.11395/aem.2.0_3.

[32] Cui H, Thomson D, Eskandari S, Petrinic N. A critical study on impact damage simulation of IM7/8552 composite laminate plate. Int J Impact Eng 2019;127:100–9. http://dx.doi.org/10.1016/j.ijimpeng.2019.01.009.

[33] Kwon J, Choi J, Huh H, Lee J. Evaluation of the effect of the strain rate on the tensile properties of carbon-epoxy composite laminates. J Compos Mater 2019;51:3197–210. http://dx.doi.org/10.1177/0021998316683439.

[34] Cui H, Yasaee M, Melro AR. Dynamic inter-fibre failure of unidirectional composite laminates with through-thickness reinforcement. Compos Sci Technol 2019;176:64–71. http://dx.doi.org/10.1016/j.compscitech.2019.04.004.